Modeling terahertz emission from the target rear side during intense laser-solid interactions

A. Woldegeorgis,[1,2,*] S. Herzer,[1] M. Almassarani,[1,2] S. Marathapalli,[1] and A. Gopal[1,2,†]
[1]*Institute of Optics and Quantum Electronics, Max-Wien platz 1, 07743 Jena, Germany*
[2]*Helmholtz Institute Jena, Fröbelstieg 3, 07743 Jena, Germany*

(Received 27 May 2019; published 25 November 2019)

Relativistic laser-solid target interaction is a powerful source of terahertz radiation where broadband terahertz radiation is emitted from the front and rear surfaces of the target. Even though several experimental works have reported the generation of subpicosecond duration gigawatt peak power terahertz pulses from the target rear surface, the underlying physical process behind their origin is still an open question. Here we discuss a numerical model that can accurately reproduce several aspects of the experimental results. The model is based on the charged particle dynamics at the target rear surface and the evolution of the charge separation field. We identify the major contributors that are responsible for broadband terahertz emission from the rear surface of the target.

DOI: 10.1103/PhysRevE.100.053204

I. INTRODUCTION

Plasmas produced during intense laser-matter interaction emit electromagnetic radiation in a broad spectral range [1–4]. This radiation can be coherent and/or incoherent depending on the generation process. In addition to being radiation sources for potential secondary applications, the characterization of the radiation itself can provide invaluable information about the spatiotemporal dynamics of the plasma sources, which are difficult to diagnose otherwise.

In this context, recent observations [5–13] of powerful terahertz (THz) radiation from laser-solid interaction have aroused great interest [14–17]. Many parameters could directly influence the emission from the front surface as the incident short pulse laser interacts with the solid target. The most dominant processes are the charge separation field generated by the ponderomotive force of the laser [18], the antenna mechanism due to the electrons generated at the focal spot driving laterally out of the target surface [19], and linear mode conversion [20]. The first observation of THz radiation from the target rear surface was reported by Gopal *et al.* in Ref. [6], where strong THz emission at large angles to the target normal direction was observed. They argued that the charge particle dynamics at the target rear surface are responsible for THz generation, as neither the interacting laser pulse nor the THz radiation generated at the front surface can go through the solid target. Later, coherent and incoherent measurement techniques were employed to record the temporal characteristics and to extract the spectral characteristics of the THz radiation. The results showed subpicosecond pulses with peak powers reaching up to the gigawatt (GW) level and a very broad spectrum containing many octaves of frequencies [7,8]. Furthermore, studies using two-dimensional (2D) particle-in-cell simulations showed rich phenomenology in the experimental results, suggesting that the charged particle dynamics at the target rear surface contribute to THz emission via numerous processes such as the electron dynamics in the sheath field, surface plasmons, surface currents, and so on. Independent studies also recorded strong THz emission and attributed their observation to transition radiation generated by the electrons exiting the rear of the target [9] and to electron reflux at the plasma sheath [10]. However, in these observations, radiation generated only in small solid angles of the rear surface were measured despite considering the emission to be symmetric. In another independent study, Poye *et al.* proposed that electromagnetic pulses in the THz range are generated by surface current created by the ejection of electrons from the target [21]. In their latest work, Herzer *et al.* investigated in detail the THz emission from the target rear surface for various laser and target parameters, and they observed that indeed there are multiple pulses with different temporal duration [11].

The polarization of the generated radiation is found to be mostly radial [11,22]. Furthermore, for an oblique angle of incidence of the interaction laser pulse, *p*-polarization results in higher THz yield than *s*-polarization [23]. Based on experimental observations, it was suggested that THz radiation from the target rear surface is mostly due to the charge particle dynamics resulting in the generation of transition radiation and sheath radiation [11]. The ambiguity in the THz generation process and the presence of multiple pulses raised further questions regarding the THz generation process. In their recent comprehensive work, Gopal *et al.* provided a full visualization of the THz beam profile along with temporal measurements and angular distribution of the electron and proton/ion spectra behind the target rear surface [24].

In this article, we present a detailed numerical investigation of THz generation using the experimentally recorded electron and ion spectra from the target rear surface. We compare the results of the numerical modeling with the experimental observations presented in [24]. Subsequently, we also estimate the longitudinal bunch duration of the particles emitted from the target rear surface and the source size of the plasma sheath generating THz radiation. The article is structured as follows. In Sec. II, a brief discussion on the generation of hot electrons

*abel.woldegeorgis@uni-jena.de
†amrutha.gopal@uni-jena.de

during laser–thin-foil interaction is presented, followed by experimentally measured energy spectra and temperature of the electrons and protons. A numerical model of the dominant THz generation mechanisms is described in Sec. III, and the experimentally recorded electron and proton/ion spectra are employed for the estimation of THz radiation. In Sec. IV, the longitudinal bunch length of the electrons is estimated from the spectra of the THz radiation.

II. HOT ELECTRON GENERATION: EXPERIMENT

During intense laser-solid interactions, hot electron bunches with charge reaching ∼nC can be generated via numerous collisionless absorption processes such as Brunel absorption, resonance absorption, and ponderomotive or $j \times B$ heating depending on the laser intensity, polarization state and temporal contrast, pulse duration, etc. [25,26]. The total number of hot electrons (N_h) is related to the laser pulse energy by the energy conservation $N_h = \eta E_L/k_B T_e$, with E_L the incident laser energy, k_B Boltzmann's constant, and T_e the average hot electron temperature. For a laser pulse with moderate intensity (between 10^{16} and 10^{18} W/cm^2) interacting with a solid target with a very steep plasma density profile where the density scale length $L_s \ll \lambda_{\text{laser}}$, the electrons are directly accelerated in the laser field via Brunel absorption [27,28], whereas in the case of $L_s \approx \lambda_{\text{laser}}$, the resonant absorption mechanism in which the laser pulse resonantly drives a plasma wave at the critical density surface dominates the hot electron generation process [29,30]. At relativistic intensities, i.e., $I \geqslant 10^{18}$ W/cm^2, the effect of the laser magnetic field can no longer be disregarded, and the hot electrons are predominantly driven by the $j \times B$ heating mechanism [23,31,32]. For our laser system (details discussed below), the dominant absorption mechanism is the $j \times B$ ponderomotive heating in which the electrons are accelerated along the laser-propagation (LP) direction [23,33,34]. However, for a p-polarized laser obliquely incident on the target and a "small" preplasma formed, a resonance absorption where the electron bunches are accelerated in the target normal (TN) direction may as well occur [29]. The scaling of the electron temperature generated by the $j \times B$ heating mechanism is given by [31] $T_{j\times B} = 0.511(\sqrt{1+a_0^2} - 1)$ MeV, with $a_0 = \sqrt{\frac{I\ (\text{W cm}^{-2})\lambda^2_{\text{laser}}\ (\mu\text{m}^2)}{1.37\times 10^{18}}}$ being the dimensionless laser parameter. On the contrary, the temperature of the electron bunch produced by resonant absorption scales with $T_{\text{res}} = 0.239 a_0^{2/3}$ MeV [30].

In thin targets, these electrons could propagate through the target and exit at the rear side and generate a strong quasistatic field, which in turn can ionize the neutral atoms and accelerate positive charges [25,35]. The dynamics of the electrons at the rear surface, including the exit from the target rear surface, sheath formation, and acceleration all leads to the emission of radiation [11,36–40]. Considering the spatiotemporal dynamics of the hot electrons and the ions, two main processes could lead to coherent emission of electromagnetic radiation from the rear surface of the target. These are as follows: (i) Transition radiation (TR) due to hot electron bunches traversing the plasma-vacuum boundary at the rear surface, and (ii) sheath radiation (SR) due to plasma sheath formation, expansion, and the resultant ion acceleration process in the target normal direction [11,24]. The energy spectrum, temperature, and angular distribution of the electrons are crucial parameters that determine the spectral (temporal) and angular (spatial) characteristics of the generated radiation. Since the spatial distribution of the electrons can also reveal the dominant electron heating mechanism at the front surface during the laser-target interaction, we recorded the energy-resolved angular distribution of the electrons along with the THz diagnostics. Additionally, the ion spectra in the target normal direction and angular distribution of the protons and ions were recorded.

The experiments were carried out at the JETI40 laser system at the Institute of Optics and Quantum Electronics at the University of Jena. JETI40 delivers a p-polarized laser pulse with energy $E_L = 650$ mJ on target with a duration $\tau_L = 30$ fs and center wavelength $\lambda_0 = 0.8$ μm. The laser pulse was focused down to a spot with a full width at half-maximum (FWHM) radius r_0 of 1.25 μm and incident onto a 5-μm-thick titanium foil at 45° producing peak intensity $I \sim 5 \times 10^{19}$ W/cm^2 (corresponding to $a_0 \approx 4.8$). The picosecond contrast of the laser is $\sim 10^{-7}$–10^{-9} in the amplified spontaneous emission (ASE) pedestal along with a prepulse (intensity level of $10^{-6}:1$) arriving ∼10 ps before the main pulse [23]. The ASE and the prepulse have sufficient intensity to start ionizing the target and create a preformed plasma prior to the arrival of the peak of the main pulse.

The electron beam profile was recorded using a Gafchromic radiochromic film (RCF) stack consisting of nine RCFs with aluminum sheets of various thicknesses arranged in between. It was placed behind the target in a semicircle angularly covering the whole back surface in the azimuthal (interaction) plane (θ_{elec}) and ±17° in the elevation plane (ϕ_{elec}). The polar plot in Fig. 1(a) represents the energy-resolved angular distribution of the electrons. The electron number is integrated for all ϕ_{elec} and plotted as a function of θ_{elec}. Low-energy electrons (< 0.25 MeV) are distributed isotropically behind the target. At higher energies, the distribution is more dominant toward the laser propagation direction (LP). The maximum energy of the electrons recorded in the TN direction is 0.575 MeV while in the LP direction it is no less than 2.25 MeV. The asymmetric spatial distribution and peak energy values in the TN and LP directions indicates the presence of multiple processes through which the electrons acquire energy from the incident laser pulse.

The energy spectra of the hot electrons for θ_{elec} of $0° \pm 10°$ and $45° \pm 10°$ are plotted in Fig. 1(b). The electron temperatures were determined from a Boltzmann function fitted on the respective experimentally measured spectra. The fits indicate that the electron bunch accelerated in the TN direction, which is ascribed to resonance absorption, has a temperature of 0.45 ± 0.05 MeV, whereas the electrons driven by the laser ponderomotive force in the LP direction exhibit a temperature of 1.75 ± 0.09 MeV. These results were compared to the electron temperatures predicted by the scaling laws for $a_0 = 4.8$. The results are 0.68 MeV for resonance absorption and 1.99 MeV for $j \times B$ heating, which are in reasonable agreement with our experiment.

The angular distribution of the proton and ion beam was recorded using a CR-39 nuclear track detector placed behind a target in a semicircle geometry subtending the entire angle in the interaction plane. Figure 2(a) presents the angular

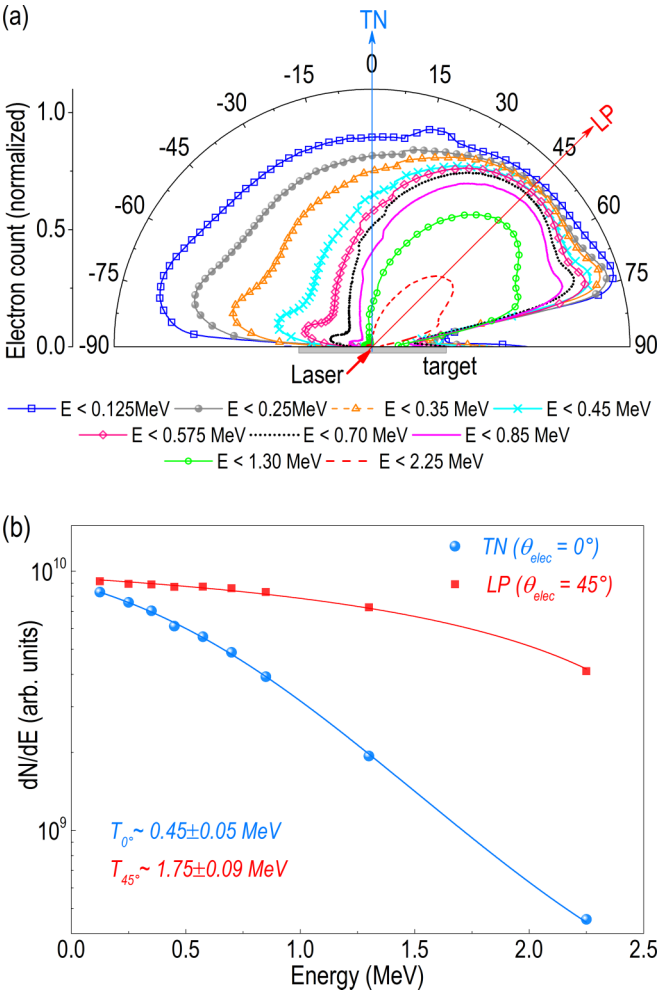

FIG. 1. (a) Energy-resolved angular distribution of hot electrons emitted at the rear surface of a 5-μm-thick titanium target. A stack of nine radiochromic films (RCFs) with aluminum foils of various thicknesses in between enabled the energy-resolved measurement. The target normal (TN) ($\theta_{\rm elec} = 0^\circ$) and laser-propagation (LP) ($\theta_{\rm elec} = 45^\circ$) direction are labeled accordingly. (b) The energy spectra of fast electrons in the TN and LP directions measured using the RCF stack (the symbols) and the corresponding temperatures estimated from the Boltzmann fit function (solid lines).

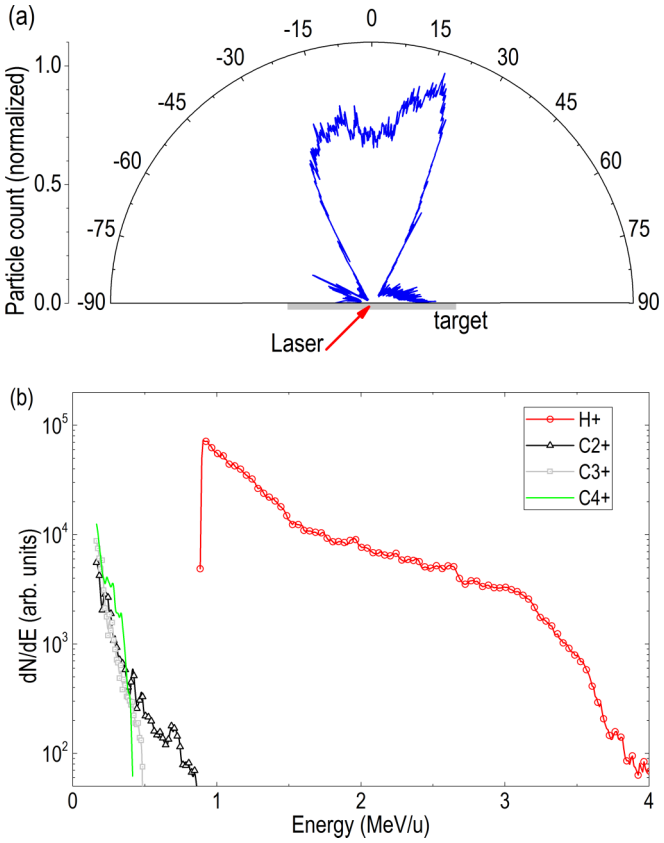

FIG. 2. (a) Angular distribution of the proton and ion beams recorded by a CR-39 nuclear tracker placed at the rear side of the target. (b) Typical energy spectra of the dominantly accelerated ions (H^+, C^{2+}, C^{3+}, and C^{4+}) measured by a Thomson parabola.

distribution of the sheath accelerated proton beam recorded by the CR-39 nuclear track. Unlike the electron beam, the proton and ion beam is only visible in the target normal direction with an opening half-angle of $23^\circ \pm 1^\circ$ suggesting that the slower electrons ejected in the TN direction are only contributing to ion acceleration. The spectra of the ions were also recorded using an ion spectrometer placed in the TN direction with an acceptance solid angle of 1 msr and presented in Fig. 2(b). The maximum proton energy recorded is ~3.8 MeV. In addition to protons, C^{2+}, C^{3+}, and C^{4+} are also present in the recorded spectrum.

With the availability of the particle spectra and the angular distribution, we can now estimate the energy and spatiotemporal characteristics of the transition radiation generated by the electrons exiting the target-rear side and the sheath radiation generated via the subsequent expansion of the plasma sheath.

III. THEORY OF THz GENERATION PROCESSES

In this section, we present the numerical estimate of two dominant THz generation mechanisms. First, radiation generated by the electrons upon exiting the target rear surface in both the target normal and laser propagation direction is calculated. Thereafter, we look at the radiation generated by the plasma sheath formation and expansion resulting in ion acceleration.

A. Coherent transition radiation

Transition radiation (TR) is emitted when a charged particle traverses a boundary between two materials with different dielectric properties [41,42]. In a scenario relevant to laser-plasma interaction where the hot electrons travel across the boundary between a plasma with dielectric constant $\epsilon_r \to -\infty$ and a vacuum ($\epsilon_r = 1$), the angular and spectral distribution of the energy of the TR by a single electron reads [40]

$$\frac{d^2\varepsilon_e}{d\omega d\Omega} = \frac{d^2\varepsilon_e^{\parallel}}{d\omega d\Omega} + \frac{d^2\varepsilon_e^{\perp}}{d\omega d\Omega}, \tag{1}$$

where the indexes $\parallel$ and $\perp$ denote the parallel and perpendicular component of the electric field of the TR with respect to the radiation plane.

The two orthogonal polarization components are given by

$$\frac{d^2\varepsilon_e^{\parallel}}{d\omega d\Omega} = \frac{e^2\beta^2\cos^2\psi}{4\pi^3\epsilon_0 c}\left[\frac{\sin\theta - \beta\sin\psi\cos\phi}{(1-\beta\sin\theta\sin\psi\cos\phi)^2 - \beta^2\cos^2\theta\cos^2\psi}\right]^2, \tag{2}$$

$$\frac{d^2\varepsilon_e^{\perp}}{d\omega d\Omega} = \frac{e^2\beta^2\cos^2\psi}{4\pi^3\epsilon_0 c}\left[\frac{\beta\cos\theta\sin\psi\sin\phi}{(1-\beta\sin\theta\sin\psi\cos\phi)^2 - \beta^2\cos^2\theta\cos^2\psi}\right]^2, \tag{3}$$

where e and β represent the charge and the reduced velocity of the electron, respectively, c is the free-space light velocity, and ψ is the electron incident angle [equivalent to θ_{elec} in Fig. 1(b)] at the boundary. θ is the angle between the direction of the emitted radiation and the observer, while ϕ represents the azimuthal angle defined in the boundary (XY) plane.

In Sec. II, it is shown that during laser-solid target interaction, copious amounts of hot electrons are generated and transported to the rear side across the target. As a result, the total energy of the emitted TR is the superposition of the radiated fields from individual electrons. For a beam of N_e electrons with a longitudinal bunch length (σ_z) crossing the plasma-vacuum boundary, the TR emitted by individual electrons adds up coherently for wavelengths, λ_{TR}, longer than σ_z and scales with $\approx N_e^2$. On the other hand, at wavelengths much shorter than σ_z, the radiation field from each of the electrons adds up incoherently and scales only with N_e. For sufficiently large N_e, the incoherent transition radiation (ITR) can be neglected. The angular and spectral distribution of the coherent component of the radiation (CTR) by the electron bunch can be calculated by [40,43]

$$\frac{d^2\varepsilon_{\text{CTR}}}{d\omega d\Omega} \approx \frac{e^2N_e^2}{4\pi^3\epsilon_0 c}\left(\left|\int d^3p\, g(p)\,\xi^{\parallel}F(\omega)D(\omega,\rho)\right|^2 + \left|\int d^3p\, g(p)\,\xi^{\perp}F(\omega)D(\omega,\rho)\right|^2\right), \tag{4}$$

where p is the electron momentum, and $g(p)$ is the electron bunch momentum distribution. $\xi^{\parallel}$ and $\xi^{\perp}$ denote the electric-field amplitudes in the plane parallel and perpendicular to the radiation plane, respectively. $F(\omega)$—the coherence function, also called the bunch form factor—is the Fourier transform (FT) of the normalized bunch distribution, whereas $D(\omega, \rho)$ represents the diffraction function incorporating the diffraction effects on the CTR spectrum arising from the finite transverse size ρ of the boundary [43]. The bunch form factor $F(\omega)$ and the diffraction function $D(\omega, \rho)$ for a boundary with lateral extension of radius $\rho = 5$ mm are calculated based on the estimated bunch dimensions (longitudinal and transverse) and the target size relevant to our experiment. The results are plotted in Fig. 3.

Figure 4 shows the angular distribution of the CTR with electric fields parallel ($\parallel$) and perpendicular ($\perp$) to the radiation plane calculated for electrons exiting the target in TN and LP directions. It can be seen that for $\theta_{\text{elec}} = 0^\circ$, there is no electric field with a $\perp$ polarization component. The CTR emitted in the TN direction is thus a purely radially polarized beam. On the other hand, the CTR generated by $\theta_{\text{elec}} = 45^\circ$ has both orthogonal components, albeit with different magnitude. The energy of the $\parallel$ component is twice that of the $\perp$ component, indicating that the radiation, although still a cylindrical vector beam, is not purely radially polarized, rather it is more like a horizontally polarized LG_{01} mode. This polarization property has been experimentally observed in [22], where a significantly stronger radial field component was measured in the laser propagation direction.

The spectrum of the CTR was calculated by incorporating the coherence and diffraction functions given in Fig. 4. The angular and spectral distributions of the CTR from $\theta_{\text{elec}} = 0^\circ$ and 45° are shown in Fig. 5. Most of the energy of the radiation is located in a spectral range <2 THz. The corresponding time domain of the CTR transients shown in Fig. 6 was obtained by performing an inverse Fourier transform (IFT) on the angularly integrated spectra. The FWHM pulse durations of the CTR-THz emissions are $\tau_{0^\circ} \approx 295$ fs and $\tau_{45^\circ} \approx 487$ fs. These numerical estimates are comparable to the experimental measurement of the THz pulse durations performed with an electro-optic technique [24]. It can be seen in Figs. 5 and 7 that the CTR emitted by these electron bunches exiting the target rear surface has a broader angular distribution due to the contribution of the enormously numerous low-energy electrons in the bunches with a Boltzmann-like distribution. The broadening is more pronounced in the CTR emission in the TN direction as most of the electrons in the $\theta_{\text{elec}} = 0^\circ$ bunch are low-energy electrons as compared to the bunch exiting at 45° (see Fig. 1). On the other hand, the asymmetry in the angular distribution of the CTR from $\theta_{\text{elec}} = 45^\circ$ can be ascribed to the oblique incidence of the bunch with respect to

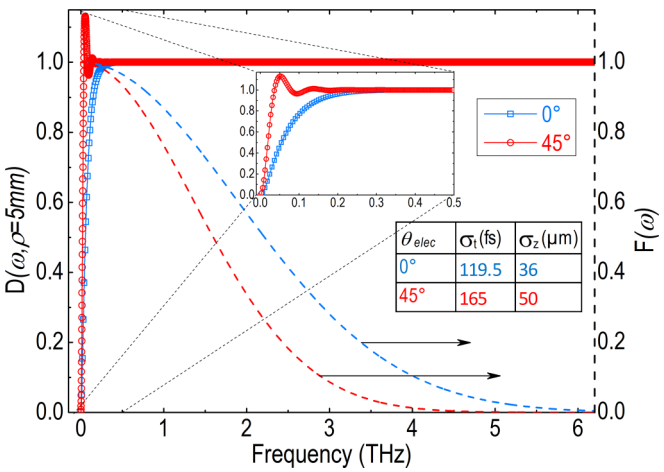

FIG. 3. The diffraction function $D(\omega, \rho)$ calculated for a transverse boundary with radius $\rho = 5$ mm and the coherence function $F(\omega)$ (right axis) calculated for the electron bunches exiting the target in the TN and LP directions from their corresponding energy spectrum. The table in the inset summarizes the estimated bunch length for the two bunches at the plasma-vacuum boundary, which critically determines the spectrum of the CTR.

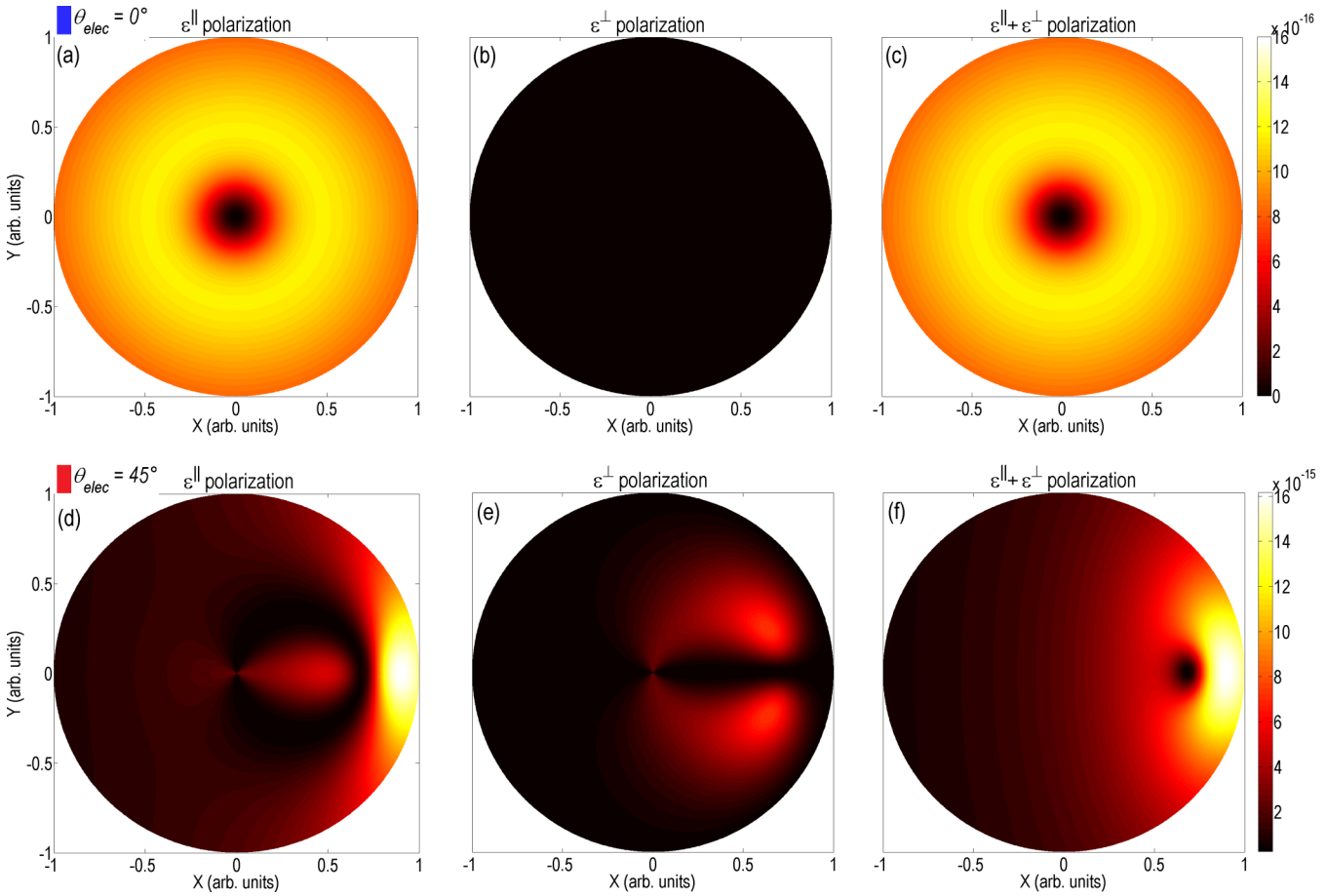

FIG. 4. Spectrally integrated angular distribution, on the XY plane, of the CTR energy for (a,d) parallel component ($\varepsilon^{\parallel}$), (b,e) perpendicular component ($\varepsilon^{\perp}$), and (c,f) the sum of the two polarization components ($\varepsilon^{\parallel} + \varepsilon^{\perp}$) for $\theta_{\rm elec} = 0^{\circ}$ (top) and 45° (bottom).

the target rear surface, and the disparity between the energy content of the two lobes is prominent for bunches with a large number of low-energy electrons. Furthermore, the detrimental effect on the CTR yield arising from the scattering of electrons due to collisions while traveling through the target material was not considered in all the calculations presented here since its effects are negligible in interactions at relativistic intensities.

B. Sheath radiation

Another mechanism that could result in the emission of coherent THz radiation during laser-solid target interaction is the sheath acceleration process. This process can be described in a simple manner as follows. A large number of hot electrons generated at the front side travel across the target reaching the rear side. The electrons escaping toward the vacuum leave the target positively charged, creating a charge imbalance that in turn results in the generation of a strong electrostatic field. This field is strong enough to trap and confine most of the escaping electrons creating a hot electron sheath. In addition, the electrostatic field ionizes the neutral atoms found at the rear surface, leading to the expansion of the plasma and acceleration of the positively charged ions in the target normal direction [35]. As seen from Fig. 2(a), the electrons exiting only in the target normal direction contribute to sheath formation and ion acceleration. The plasma expansion model indicates, at the onset of expansion, that the quasineutrality is violated at the front of the expanding plasma sheath, i.e., $n_{e,\rm fr} \neq n_{p,\rm fr}$, where $n_{e,\rm fr}$ and $n_{p,\rm fr}$ are the electron and proton densities at the plasma front, respectively [44–46]. This results in a current that is equivalent to a net uncompensated charge moving away from the target. Since the evolution of the sheath field is transient, the dynamics of the moving net charge can be considered as a transient electric dipole and could give rise to a dipolelike emission of electromagnetic radiation.

Here we assume the sheath to be a pure electron-proton plasma expanding in z or TN-direction. The velocity of the expanding plasma front v_f as a function of time t is calculated to be [44]

$$v_f(t) = 2c_s \ln(\tau^2 + \sqrt{1+\tau^2}), \tag{5}$$

where $c_s = (k_B T_e/m_p)^{1/2}$ is the sound or acoustic velocity and $\tau = \omega_{\rm pp} t/\sqrt{2e_N}$ is the normalized acceleration time, with $\omega_{\rm pp}$ being the proton plasma frequency and $e_N = \exp(1) = 2.718\,28\ldots$. Initially the plasma front expands with velocity v_f, which increases steadily with time, until $t = \tau_0 = \sqrt{2e_N}/\omega_{\rm pp}$. Afterward, for $t > \tau_0$, the acceleration is small and we can consider the plasma front to be moving with uniform velocity.

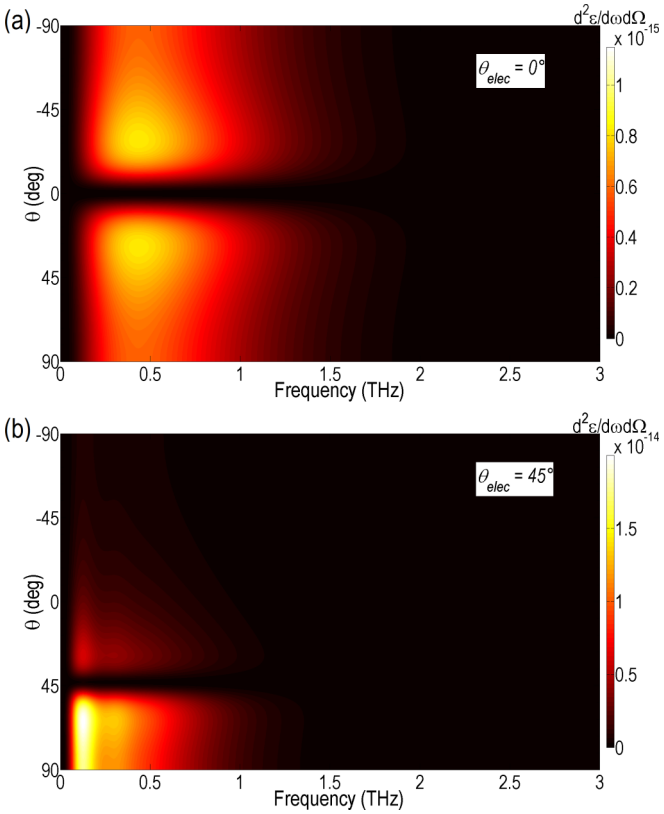

FIG. 5. Angular distribution of the energy of different spectral components of the CTR emission by a hot electron bunch leaving the rear surface in (a) the TN ($\theta_{\rm elec} = 0^\circ$) direction and (b) the LP ($\theta_{\rm elec} = 45^\circ$) direction.

The changes in the electron and proton densities at the expanding plasma front are given by [44]

$$n_{e,\rm fr}(t) = \frac{2n_{e0}}{2e_N + \omega_{\rm pp}^2 t^2} = \frac{n_{e0}}{e_N(1+\tau^2)}, \tag{6}$$

$$n_{p,\rm fr}(t) = \frac{4n_{e0}}{2e_N + \omega_{\rm pp}^2 t^2} = \frac{2n_{e0}}{e_N(1+\tau^2)}, \tag{7}$$

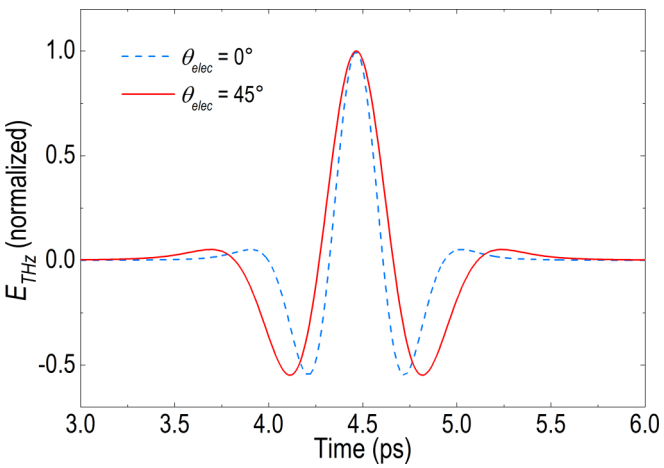

FIG. 6. Time-domain representation of the THz pulses produced by the electrons leaving the target rear surface at incident angles 0° and 45°.

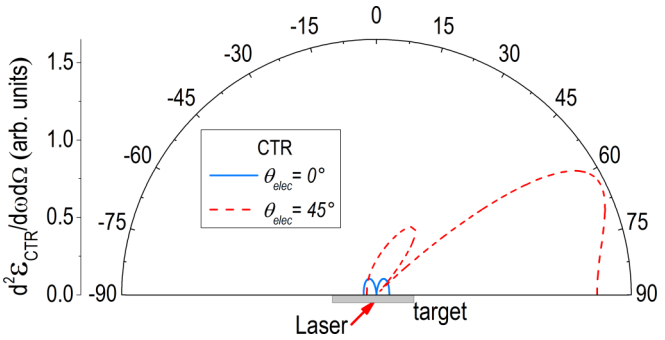

FIG. 7. Angular distribution of the CTR generated in the radiation plane ($\phi = 0^\circ$) by hot electron bunches crossing the plasma-vacuum boundary at 0° and 45°.

with $n_{e0} = \frac{N_h}{\pi r_0^2 c\tau_L}$ being the electron density in the unperturbed plasma. The time-dependent charge density distribution and the plasma current distribution can thus be expressed as follows:

$$\rho(r,z,t) = e[n_{e,\rm fr}(z,t) - n_{p,\rm fr}(z,t)]\exp(-r^2/R^2), \tag{8}$$

$$j(r,z,t) = -v_f(t)\delta(z - v_f t + \lambda_D)\rho(r,z,t) \tag{9}$$

with $\lambda_D = (\frac{\epsilon_0 k_B T_e}{e^2 n_{e,\rm fr}})^{1/2}$ the longitudinal extension of the sheath, and R is the lateral radius of the sheath in the transverse direction conditioned by the laser focal spot radius r_0, for our case $r_0 \approx 1.25\ \mu$m, and the half-angle α of the electron emission, which is obtained from the spatial distribution of the proton beam [from Fig. 2(a), $\alpha \approx 23^\circ$] and target thickness d: $R = r_0 + d\tan\alpha \approx 3.4\ \mu$m. The density distribution of the electrons in the sheath can be taken as Gaussian, considering the Gaussian nature of the intensity and temporal profile of the focused laser, and their mean energy at a defined location can be taken to be radially homogeneous [47].

The transient dynamics of the plasma sheath can emit radiation and can be calculated from the Lienard-Wiechert potential [48]. For an observer far from the plasma current source ($r \gg \lambda_D$), the near-field term can be neglected and only the radiation term (far field), which comes from accelerated charges, is present. The electric field ξ of the radiated wave can be obtained as

$$\xi(\mathbf{r},t) = \frac{1}{4\pi\epsilon_0}\int(d\mathbf{r}')\left[\frac{\mathbf{n}}{cr}\frac{d}{dt}\{\rho(\mathbf{r}',t')\}_{\rm ret} \cdots - \frac{1}{c^2 r}\frac{d}{dt}\{j(\mathbf{r}',t')\}_{\rm ret}\right]. \tag{10}$$

The source terms on the right-hand side of the above equation are the spatiotemporal distributions of the charge density ρ and plasma current j given by Eqs. (10) and (11). For charge and current densities with arbitrary time dependence, as is the case here, solving the radiation fields in the frequency domain is favorable due to dispersion and retardation. Therefore, we write the electric field in Fourier space as

$$\xi(\mathbf{r},\omega) = -k(\omega)\frac{qc_s\sin\theta}{4\pi\epsilon_0 rc}\exp[ik(\omega)r]F(\omega,\theta), \tag{11}$$

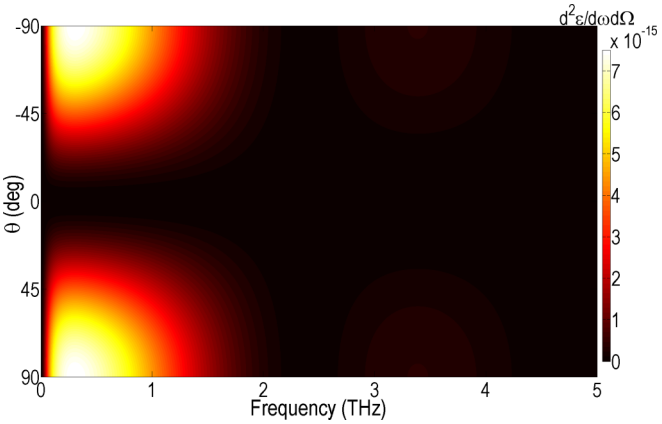

FIG. 8. Spectral and angular distribution of the energy of the SR. Most of the radiation is emitted in the 0.1–1.5 THz spectral range and in the direction normal to the direction of acceleration.

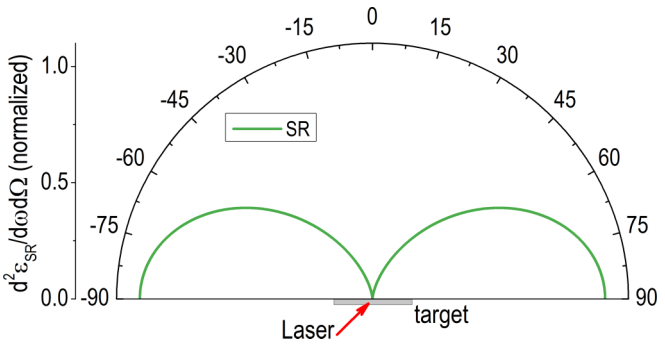

FIG. 9. Angular distribution of the SR emitted by the plasma sheath with uncompensated net charge expanding in the z-direction.

where $k(\omega) = \frac{\omega}{c}$ and $q = e\rho V_{\text{sheath}}$ is the net charge in the sheath with the sheath volume calculated as $V_{\text{sheath}} = \pi R^2 \lambda_D$. The sheath radiation (SR) emitted during the expansion of the plasma into the vacuum is estimated from the sheath parameters, such as spatial extension, charge density, and velocity of the expanding plasma front. Accordingly, the radiated energy of the SR (ε_{SR}) per angular frequency and solid angle can be derived from Eq. (11) and is given by [48]

$$\frac{d^2\varepsilon_{\text{SR}}}{d\omega d\Omega} = \frac{c\epsilon_0 r^2}{\pi\omega^2}|\xi(\omega)|^2 = \frac{q^2 c_s^2}{4\pi^3\epsilon_0 c^3}|F(\omega,\theta)|^2 \sin^2\theta, \quad (12)$$

where $F(\omega,\theta)$ is the form factor and can be expressed by [49]

$$F(\omega,\theta) = \frac{i\omega\tau_0[1-\exp(-1-i\omega\tau_0)]}{(1+\omega\tau_0)^2}\exp\left(-\frac{\omega^2 R^2 \sin^2\theta}{4c^2}\right). \quad (13)$$

Figure 2 depicts the angular distribution of the sheath accelerated proton beam recorded by a CR39 nuclear track detector placed behind a target. Analysis of the beam profile reveals that protons were accelerated only in the TN direction with a half-angle opening of $(23 \pm 1)^\circ$. As a result, the radiation emitted during the sheath acceleration process was calculated by using the electron energy spectra and temperature of the bunch propagating in the TN direction in Eq. (12). The angular and spectral distribution of SR is shown in Fig. 8. It is evident that most of the radiation is emitted in large angles with respect to the target normal, and the spectra of the emitted radiation are mostly below 2 THz. Spectrally integrated angular distribution of the SR radiation is shown in Fig. 9. Unlike CTR, the SR is predominantly emitted in wide angles with respect to the direction of acceleration and deceleration of the charged particles (z-direction). The temporal waveform is extracted by performing IFT on the angularly integrated SR spectrum, and the result shows that the FWHM pulse duration of the transient $\tau_{\text{SR}} \approx 350$ fs. We may compare it with the experimentally measured value of the sheath radiation presented in [24] 371 ± 30 fs. Independently, we can also estimate the time required for the quasistatic field $E_0 = k_B T_e/e\lambda_D \approx 0.9$ TV/m to accelerate the protons to the recorded maximum kinetic energy of 3.8 MeV, and it is found to be $\approx 322 \pm 9$ fs. On the other hand, the empirically estimated acceleration time given by t_{acc} (fs) $= 1.3(\tau_L + 60)$ [50] is only 117 fs for the given experimental parameters.

Let us now compare the energy of the radiation emitted by the two processes. Results of the numerical estimates presented in Figs. 5 and 8 point out that the strongest emission is CTR emitted by the electrons exiting in the LP (45°) direction. SR radiation due to plasma expansion or particle acceleration is a factor of 2 lower. On the contrary, the CTR emission by the electrons exiting in the TN direction is an order of magnitude smaller. Furthermore, their temporal structures reveal different pulse durations and thereby different spectral content. Comparing these numerical estimates based on the particle spectrum to the experimental measurements of the THz radiation presented in [24], the following conclusions can be made. First, the temporally integrated THz beam profile is asymmetric with most of the radiation localized in the laser propagation direction agreeing well with the numerical estimates. Moreover, the presence of multiple peaks also implies the presence of different generation mechanisms. This argument can be verified from the temporal measurements using the electro-optic (EO) diagnostic. It shows the presence of multiple pulses with different pulse durations and temporal delays. As mentioned before, the numerically estimated values of the three emission processes are 295 and 487 fs for CTR emissions and 350 fs for SR emission. Comparing it with the EO measurements, the values are 331 ± 25, 308 ± 27, and 379 ± 45 fs, respectively. Also combining these results with the amplitudes of the detected pulses, they can be chronologically identified as initial emission due to CTR in the 0° followed by 45° and finally SR emission.

IV. BUNCH LENGTH ESTIMATION

The longitudinal length of an ultrashort electron bunch can be measured or monitored by employing a variety of techniques, such as transverse deflecting structures [51], directly reconstructing the longitudinal length from the spectrum of the coherent transition, diffraction, or synchrotron radiation emitted by the bunch itself [52], etc. So we can employ the results from the experimentally observed CTR temporal waveforms obtained from single-shot electro-optic (EO) detection. The minimum pulse duration that can be measured using this technique is defined by the crystal response function [11], which in our case was 103 fs. Hence it is valid to assume that

the experimentally recorded temporal duration is the actual pulse duration of the radiation. The CTR spectrum, which is obtained from the FT of the temporal waveform, is determined by the form factor $F(\omega)$ (which sets the high cutoff frequency) and the diffraction effects (which set the low cutoff). The longitudinal bunch length σ_z can then be inferred from the analyzed CTR spectrum.

As presented in Sec. III A, the CTR spectrum is predominantly determined by $F(\omega)$ or σ_z of the electron bunch at the plasma-vacuum boundary. In characterizing the CTR emitted by the multiple fast electron bunches, their σ_z at the target rear surface was estimated from initial parameters at the target front surface conditioned by the laser pulse and the measured energy-resolved angular distribution of the electrons. Here in this section, we estimated σ_z from the experimentally measured CTR spectrum reported in [24], and the results are compared with the values estimated in Sec. III A. In Ref. [24], the temporal measurement of the THz radiation revealed the existence of three different pulses whose origin is attributed to the generation mechanisms discussed in Sec. III of this article. Here we consider the pulses 1 and 2 generated by the CTR process.

The bunch form factor for an uncorrelated spatial distribution is expressed as $F(\omega) = F^{\parallel}(\omega)F^{\perp}(\omega)$, where $F^{\perp}$ is associated with the transverse distribution and $F^{\parallel}$ is associated with the longitudinal profile. The fast electron bunches generating the CTR can be assumed to have a Gaussian spatial profile, and the form factor (since the lateral size $\sigma_r << \sigma_z$) can be simplified to [53]

$$F(\omega) \sim \exp\left(-\frac{\omega^2\sigma_z^2}{c^2}\right) \tag{14}$$

with $\omega = 2\pi\nu$.

To establish a relation between the CTR spectrum and σ_z, the spectral width $\sigma_{\rm rms}$ of the CTR can be determined by fitting a Gaussian function, on the CTR spectrum, with a form

$$g(\nu) \sim \exp\left(-\frac{(\nu-\nu_c)^2}{2\sigma_{\rm rms}^2}\right). \tag{15}$$

By equating the fit function $g(\nu)$ with the form factor (taking $\nu_c = 0$), an analytical expression relating the spectral width $\sigma_{\rm rms}$ with the bunch size σ_z can be derived [54] and reads

$$\sigma_z \approx \frac{1}{2\sqrt{2}\pi}\left(\frac{c}{\sigma_{\rm rms}}\right). \tag{16}$$

We determined the rms spectral width from the Gaussian function fitted on the measured CTR spectra, and the bunch length was estimated accordingly. The spectra and the fit functions are plotted in Fig. 10. As mentioned before, the spectrum of the CTR is also influenced by diffraction effects, due to the finite size of the boundary, which in particular distorts and suppresses the low-frequency components. To reliably estimate the bunch length by means of a Gaussian fit to the CTR spectrum, the latter should not be significantly distorted in the region $\nu \gg \sigma_{\rm rms}$. As can be seen in Fig. 10, the spectral region higher than $\sigma_{\rm rms}^{\rm pulse1} = 0.552$ THz and $\sigma_{\rm rms}^{\rm pulse2} = 0.825$ THz is only weakly distorted, confirming the reliability of the bunch length estimation. The calculated results from the CTR and the estimated values from the electron energy spectra are summarized in Table I.

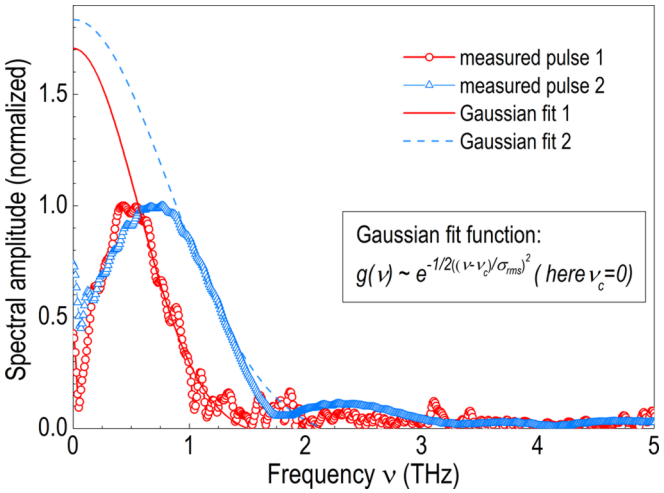

FIG. 10. Measured spectra of CTR pulses (symbols) and the corresponding Gaussian fit functions (solid lines). σ_z was estimated from $\sigma_{\rm rms}$ using Eq. (16).

The rms bunch sizes obtained by fitting a Gaussian function on the measured CTR spectra are 41 and 61 μm, whereas the ones estimated from the measured energy spectra of the hot electrons are approximately 36 and 50 μm. The reasonable agreement between the estimations further confirms the notion that the temporal property of electron bunches generated during laser-solid interaction can be inferred from the spectral characteristics of the CTR emitted by the bunches.

V. DISCUSSION AND SUMMARY

The numerical calculations to estimate the spectral and angular distribution of the THz emissions due to CTR and SR provide characteristic features of the respective generation processes. Regarding the CTR, the angular distribution of the fast electrons exiting the target reveals the presence of two distinct electron heating mechanisms, viz. resonant absorption and $j \times B$ ponderomotive heating, which generate two hot electron bunches with different temperatures and propagating in the TN and the LP direction, respectively. The yield of the CTR, which strongly depends on the energy and number of particles, generated by the LP ($\theta_{\rm elec} = 45^\circ$) electron bunch, is an order of magnitude higher than the one emitted in the

TABLE I. Summary of the bunch length σ_z estimated from the CTR spectra and from the hot electron energy spectra.

From CTR spectra:		
Pulse	$\sigma_{\rm rms}$ (THz)	σ_z (μm)
1	0.552	61
2	0.825	41
From hot electron spectra:		
$\theta_{\rm elec}$		σ_z (μm)
45°		50
0°		36

TN direction. Most of the energy of the CTR radiation lies in the spectral range between 0.1 and 1.5 THz. The low-energy electrons emitted in the TN direction generate symmetrically distributed CTR, while the contribution from the energetic electrons emitted in the LP direction is more skewed toward the target surface than TN. This results in a more asymmetric beam profile of the CTR emission in the THz band for oblique incidence of the interaction laser at relativistic intensities. Moreover, the longitudinal bunch duration (σ_z) of the two fast electron bunches was estimated from the measured CTR spectrum [24] and compared to the values obtained from the hot electron spectra. Reasonable agreement between the two estimates suggests that CTR in the terahertz range is a creditable diagnostic for particle bunches generated during laser matter interaction.

On the other hand, the contribution from the transient dynamics of the expanding plasma sheath formed at the rear surface is predominantly emitted in the noncollinear direction. The SR spectrum mostly contains frequencies below 2 THz.The plasma sheath expansion model considers the expansion to be only in the z direction and is expected to fail at accurately describing phenomena taking place in three dimensions. However, the 1D model suffices in describing the expansion for a time interval $t \leqslant t_{\mathrm{acc}}$, in which the radiation is emitted by the accelerating uncompensated dipole, since the 3D effects will not play a significant role for longitudinal expansion z_{front} shorter than the lateral sheath size R [47,55,56]. At $t = t_{\mathrm{acc}}$, the plasma front propagates $z_{\mathrm{front}} \approx \lambda_D \approx 0.53\ \mu\mathrm{m} << R\ (\approx 3.4\ \mu\mathrm{m})$, justifying the use of the 1D model in the radiation generation mechanism.

Summing up the contributions from all processes, it can be seen that the coherent THz radiation generated from the target rear surface is mostly emitted in wide angles with respect to the TN direction and is asymmetric for the oblique angle of incidence of the interaction laser. Comparing the experimentally observed THz beam profile [24], the angular distribution of the THz radiation calculated from the particle bunches agrees well. Further confirmation is also provided by the measurements of the THz transients using electro-optic measurements [24] exhibiting the presence of three THz pulses of different amplitude and temporal duration. Radiation due to other physical processes, such as the emission of low-frequency (∼1 GHz) electromagnetic pulses due to target charging, as reported by [21,57], in which the electrons flow in the radial direction toward the region where the fast electrons escape the target, was not observed in the beam profile or the EO measurement of the rear-side THz emission [24]. Moreover, the spectral analysis of the THz pulses consistently showed similar frequency content independent of the target foil size—revealing that target charging is not among the dominant THz generation mechanisms at the rear surface of a target irradiated by ultrashort intense laser pulses. Irrespective of the laser parameters and interaction conditions, we clearly show here with a complete picture of the THz emission (spatial and temporal) and particle spectra (beam profile and spectra) that there is more than one process responsible for powerful, coherent, and broadband terahertz radiation.

Thus it is evident that based on the ion and electron spectra, the spatial and spectral characteristics of the THz emission from the target rear surface can be calculated and vice versa. This provides a unique opportunity and an independent novel diagnostic to investigate and understand the charge particle dynamics during high-power laser matter interaction for various laser and interaction conditions [9,10,27,30,32–34,58–60] where different absorption mechanisms may dominate, which in turn will change the angular beam profile of the THz.

In summary, our work presented numerical models that explain several aspects of THz generation from the target rear surface during high-power laser-solid interaction. Two dominant physical processes that could give rise to coherent THz emission were identified. In addition, analyzing the spatial, temporal, and spectral properties of the terahertz pulses reveals certain characteristics, such as the longitudinal bunch length of the particle beam that generated them. This implies that the coherent terahertz emission can be well characterized without the need to describe in detail all the complex laser-target interaction processes.

[1] M. M. Murnane, H. C. Kapteyn, M. D. Rosen, and R. W. Falcone, Science **251**, 531 (1991).

[2] J. J. Macklin, J. D. Kmetec, and C. L. Gordon, Phys. Rev. Lett. **70**, 766 (1993).

[3] I. Watts, M. Zepf, E. L. Clark, M. Tatarakis, K. Krushelnick, A. E. Dangor, R. M. Allott, R. J. Clarke, D. Neely, and P. A. Norreys, Phys. Rev. Lett. **88**, 155001 (2002).

[4] J. D. Kmetec, C. L. Gordon, J. J. Macklin, B. E. Lemoff, G. S. Brown, and S. E. Harris, Phys. Rev. Lett. **68**, 1527 (1992).

[5] C. Li, M. L. Zhou, W. J. Ding, F. Du, F. Liu, Y. T. Li, W. M. Wang, Z. M. Sheng, J. L. Ma, L. M. Chen *et al.*, Phys. Rev. E **84**, 036405 (2011).

[6] A. Gopal, T. May, S. Herzer, A. Reinhard, S. Minardi, M. Schubert, U. Dillner, B. Pradarutti, J. Polz, T. Gaumnitz *et al.*, New J. Phys. **14**, 083012 (2012).

[7] A. Gopal, S. Herzer, A. Schmidt, P. Singh, A. Reinhard, W. Ziegler, D. Brömmel, A. Karmakar, P. Gibbon, U. Dillner *et al.*, Phys. Rev. Lett. **111**, 074802 (2013).

[8] A. Gopal, P. Singh, S. Herzer, A. Reinhard, A. Schmidt, U. Dillner, T. May, H.-G. Meyer, W. Ziegler, and G. G. Paulus, Opt. Lett. **38**, 4705 (2013).

[9] G. Q. Liao, Y. T. Li, Y. H. Zhang, H. Liu, X. L. Ge, S. Yang, W. Q. Wei, X. H. Yuan, Y. Q. Deng, B. J. Zhu *et al.*, Phys. Rev. Lett. **116**, 205003 (2016).

[10] Z. Jin, H. B. Zhuo, T. Nakazawa, J. H. Shin, S. Wakamatsu, N. Yugami, T. Hosokai, D. B. Zou, M. Y. Yu, Z. M. Sheng *et al.*, Phys. Rev. E **94**, 033206 (2016).

[11] S. Herzer, A. Woldegeorgis, J. Polz, A. Reinhard, M. Almassarani, B. Beleites, F. Ronneberger, R. Grosse, G. G. Paulus, U. Hübner *et al.*, New J. Phys. **20**, 063019 (2018).

[12] H. B. Zhuo, S. J. Zhang, X. H. Li, H. Y. Zhou, X. Z. Li, D. B. Zou, M. Y. Yu, H. C. Wu, Z. M. Sheng, and C. T. Zhou, Phys. Rev. E **95**, 013201 (2017).

[13] C. Li, Y.-Q. Cui, M.-L. Zhou, F. Du, Y.-T. Li, W.-M. Wang, L.-M. Chen, Z.-M. Sheng, J.-L. Ma, X. Lu *et al.*, Opt. Exp. **22**, 11797 (2014).

[14] I. Tudosa, C. Stamm, A. B. Kashuba, F. King, H. C. Siegmann, J. Stöhr, G. Ju, B. Lu, and D. Weller, Nature (London) **428**, 831 (2004).

[15] C. H. Back, D. Weller, J. Heidmann, D. Mauri, D. Guarisco, E. L. Garwin, and H. C. Siegmann, Phys. Rev. Lett. **81**, 3251 (1998).

[16] L. J. Wong, A. Fallahi, and F. X. Kärtner, Opt. Express **21**, 9792 (2013).

[17] E. A. Nanni, W. R. Huang, K.-H. Hong, K. Ravi, A. Fallahi, G. Moriena, R. J. Dwayne Miller, and F. X. Kürtner, Nat. Commun. **6**, 8486 (2015).

[18] H. Hamster, A. Sullivan, S. Gordon, W. White, and R. W. Falcone, Phys. Rev. Lett. **71**, 2725 (1993).

[19] A. Sagisaka, H. Daido, S. Nashima, S. Orimo, K. Ogura, M. Mori, A. Yogo, J. Ma, I. Daito, A. S. Pirozhkov *et al.*, Appl. Phys. B **90**, 373 (2008).

[20] Z. M. Sheng, K. Mima, J. Zhang, and H. Sanuki, Phys. Rev. Lett. **94**, 095003 (2005).

[21] A. Poyè, S. Hulin, M. Bailly-Grandvaux, J.-L. Dubois, J. Ribolzi, D. Raffeshn, M. Bardon, F. Lubrano-Lavaderci, E. D'Humières, J. J. Santos *et al.*, Phys. Rev. E **91**, 043106 (2015).

[22] A. Woldegeorgis, T. Kurihara, M. Almassarani, B. Beleites, R. Grosse, F. Ronneberger, and A. Gopal, Optica **5**, 1474 (2018).

[23] A. H. Woldegeorgis, B. Beleites, F. Ronneberger, R. Grosse, and A. Gopal, Phys. Rev. E **98**, 061201(R) (2018).

[24] A. Gopal, A. Woldegeorgis, S. Herzer, and M. Almassarani, Phys. Rev. E **100**, 053203 (2019).

[25] P. Gibbon, *Short Pulse Laser Interaction with Matter* (Imperial College Press, London, 2005).

[26] A. Macchi, M. Borghesi, and M. Passoni, Rev. Mod. Phys. **85**, 751 (2013).

[27] L. Labate, M. Galimberh, A. Giulietti, D. Giulietti, P. Köster, P. Tomassini, and L. A. Gizzi, Appl. Phys. B **86**, 229 (2007).

[28] F. Brunel, Phys. Rev. Lett. **59**, 52 (1987).

[29] W. L. Kruer, *Physics of Laser Plasma Interactions* (Addison-Wesley, Menlo Park, CA, 1988).

[30] F. N. Beg, A. R. Bell, A. E. Dangor, C. N. Danson, A. P. Fews, M. E. Glinsky, B. A. Hammel, P. Lee, P. A. Norreys, and M. Tatarakis, Phys. Plasmas **4**, 447 (1997).

[31] S. C. Wilks, W. L. Kruer, M. Tabak, and A. B. Langdon, Phys. Rev. Lett. **69**, 1383 (1992).

[32] B. I. Cho, J. Osterholz, A. C. Bernstein, G. M. Dyer, A. Karmakar, A. Pukhov, and T. Ditmire, Phys. Rev. E **80**, 055402(R) (2009).

[33] P. K. Singh, Y. Q. Cui, A. Adak, A. D. Lad, G. Chatterjee, P. Brijesh, Z. M. Sheng, and G. R. Kumar, Sci. Rep. **5**, 17870 (2015).

[34] Y. Ping, R. Shepherd, B. F. Lasinski, M. Tabak, H. Chen, H. K. Chung, K. B. Fournier, S. B. Hansen, A. Kemp, D. A. Liedahl *et al.*, Phys. Rev. Lett. **100**, 085004 (2008).

[35] S. C. Wilks, A. B. Langdon, T. E. Cowan, M. Roth, M. Singh, S. Hatchett, M. H. Key, D. Pennington, A. MacKinnon, and R. A. Snavely, Phys. Plasmas **8**, 542 (2001).

[36] J. J. Santos, F. Amiranoff, S. D. Baton, L. Gremillet, M. Koenig, E. Marhnolli, M. R. L. Gloahec, C. Rousseaux, D. Batani, A. Bernardinello *et al.*, Phys. Rev. Lett. **89**, 025001 (2002).

[37] J. Zheng, K. A. Tanaka, T. Miyakoshi, Y. Kitagawa, R. Kodama, T. Kurahashi, and T. Yamanaka, Phys. Plasmas **10**, 2994 (2003).

[38] H. Popescu, S. D. Baton, F. Amiranoff, C. Rousseaux, M. R. L. Gloahec, J. J. Santosa, L. Gremillet, M. Koenig, E. Marhnolli *et al.*, Phys. Plasmas **12**, 063106 (2005).

[39] S. D. Baton, J. J. Santos, F. Amiranoff, H. Popescu, L. Gremillet, M. Koenig, E. Marhnolli, O. Guilbaud, C. Rousseaux, M. R. L. Gloahec *et al.*, Phys. Rev. Lett. **91**, 105001 (2003).

[40] C. Bellei, S. R. Nagel, S. Kar, A. Henig, S. Kneip, C. Palmer, A. Sävert, L. Willingale, D. Carroll, B. Dromey *et al.*, Plasma Control. Fusion **54**, 035011 (2012).

[41] V. L. Ginzburg and I. M. Frank, Zh. Eksp. Teor. Fiz. **16**, 15 (1946).

[42] M. L. Ter-Mikaelian, *High-Energy Electromagnetic Processes in Condensed Media* (Wiley-Interscience, New York, 1972).

[43] C. B. Schroeder, E. Esarey, J. van Tilborg, and W. P. Leemans, Phys. Rev. E **69**, 016501 (2004).

[44] P. Mora, Phys. Rev. Lett. **90**, 185002 (2003).

[45] P. Mora, Phys. Rev. E **72**, 056401 (2005).

[46] J. Schreiber, F. Bell, F. Grüner, U Schramm, and M Geissler, Phys. Rev. Lett. **97**, 045005 (2006).

[47] P. Antici, J. Fuchs, M. Borghesi, L. Gremillet, T. Grismayer, Y. Sentoku, E. dHumières, C. A. Cecchetti, A. Mančić, A. C. Pipahl *et al.*, Phys. Rev. Lett. **101**, 105004 (2008).

[48] J. D. Jackson, *Classical Electrodynamics*, 3rd ed. (Wiley, New York, 1999), Chap. 14.

[49] A. S. Kuratov, A. V. Brantov, Y. M. Aliev, and V. Y. Bychenkovba, Quantum Electron. **46**, 1023 (2016).

[50] M. S. Schollmeier, Ph.D. thesis, TU Darmstadt, Darmstadt (2008).

[51] M. Röhrs, C. Gerth, H. Schlarb, B. Schmidt, and P. Schmuser, Phys. Rev. ST Accel. Beams **12**, 050704 (2009).

[52] U. Happek, A. J. Sievers, and E. B. Blum, Phys. Rev. Lett. **67**, 2962 (1991).

[53] J. van Tilborg, C. B. Schroeder, E. Esarey, and W. P. Leemans, Laser Part. Beams **22**, 415 (2004).

[54] M. Castellano, A. Cianchia, G. Orlandi, and V. A. Verzilov, Nucl. Instrum. Methods A **435**, 297 (1999).

[55] S. N. Chen, A. P. L. Robinson, P. Anhci, E. Brambrink, E. d'Humières, S. Gaillard, T. Grismayer, A. Mancic, P. Mora, L. Romagnani *et al.*, Phys. Plasmas **21**, 023119 (2014).

[56] L. Romagnani, J. Fuchs, M. Borghesi, P. Anhci, P. Audebert, F. Ceccherini, T. Cowan, T. Grismayer, S. Kar, A. Macchi *et al.*, Phys. Rev. Lett. **95**, 195001 (2005).

[57] C. G. Brown, Jr., A. Throop, D. Eder, and J. Kimbrough, J. Phys.: Conf. Ser. **112**, 032025 (2008).

[58] F. Brandl, G. Pretzler, D. Habs, and E. Fill, Europhys. Lett. **161**, 632 (2003).

[59] S. Ter-Avetisyan, M. Schnürer, T. Sokollik, P. V. Nickles, W. Sandner, H. R. Reiss, J. Stein, D. Habs, T. Nakamura, and K. Mima, Phys. Rev. E **77**, 016403 (2008).

[60] H. Liu, G.-Q. Liao, Y.-H. Zhang, B.-J. Zhu, Z. Zhang, Y.-T. Li, G. G. Scott, D. R. Rusby, C. Armstrong, E. Zemaityte *et al.*, Rev. Sci. Instrum. **89**, 083302 (2018).